Journal of Alloys and Compounds 923 (2022) 166449

Contents lists available at ScienceDirect

Journal of Alloys and Compounds

journal homepage: www.elsevier.com/locate/jalcom

Research article

Pyrochlore-like ZrO_2-PrO_x compounds: The role of the processing atmosphere in the stoichiometry, microstructure and oxidation state

L. Grima, J.I. Peña, M.L. Sanjuán*

Instituto de Nanociencia y Materiales de Aragón, Universidad de Zaragoza-CSIC, Facultad de Ciencias, Universidad de Zaragoza, 50009 Zaragoza, Spain

ARTICLE INFO

Article history:
Received 23 March 2022
Received in revised form 11 July 2022
Accepted 20 July 2022
Available online 21 July 2022

Keywords:
Ceramics
Oxide materials
Laser processing
Microstructure
Oxidation
Phase diagrams ZrO2–PrOx
Phase diagram
Processing atmosphere
Praseodymium oxidation
Pyrochlores

ABSTRACT

The object of this work is to study the relation between composition, microstructure and oxidation state of $Pr_{2\pm x}Zr_{2\mp x}O_{7\pm y}$ materials produced by the laser–floating zone (LFZ) technique. Three compositions are studied, nominally $Pr_{1.7}Zr_{2.3}O_{7+y}$, $Pr_2Zr_2O_{7+y}$ and $Pr_{2.24}Zr_{1.76}O_{7\pm y}$, all within the pyrochlore field in the ZrO_2–PrO_x phase diagram. Samples have been processed under four different atmospheres (O_2, air, N_2 and 5%H_2(Ar)), so as to vary the environmental conditions from oxidising to reducing. Sample colouration ranged from dark brown to bright green, owing to varying Pr^{4+} content. A close correlation is found between the phase homogeneity, the microstructure and the Pr content. Pr–deficient samples present a homogeneous microstructural aspect and composition, whereas Pr–rich compositions always break into 5–25 μm–sized grains with pyrochlore phases at the grain centre and ill–crystallised, Pr–rich oxidised phases at the grain–boundaries. Raman spectroscopy shows that different types of oxygen disorder occur depending on composition and processing atmosphere: in Pr–poor samples oxygen interstitials are created to compensate for Zr^{4+} excess charge, whereas in Pr–rich samples oxygen disorder occurs around the Pr^{3+} or Pr^{4+} ions substituting for Zr^{4+}, because of size–mismatch. Magnetic measurements showed a high Pr^{4+} content, which has been attributed to several factors: the highly oxidised state of the feedstock material, the segregation of Pr and O–rich grain boundaries in compositions with praseodymium molar rate > 0.5, and the lower oxide–ion conductivity for PZO compositions, compared to either Pr–poor or Pr–rich compositions. Post–processing thermal annealing in a vacuum at 1000 °C enabled total Pr reduction, with the exception of the Pr–rich P2.24 samples, where some Pr^{4+} ions remained in the oxidised state.

1. Introduction

Cerium–related oxides are currently used in many applications such as three–way catalysts for exhaust gas conversion or air pollution abatement, hydrogen production, solid oxide fuel cells, etc. (see Ref. [1] and references therein). Applications based on the behaviour of ceria as oxygen storage compound (OSC) rely on the redox reaction, $2Ce^{4+} + O_O^x \leftrightarrows 2Ce^{3+} + ½O_2(g) + V_O^{\bullet\bullet}$, where O_O^x and $V_O^{\bullet\bullet}$ stand for a lattice oxygen ion and vacancy, respectively, in Kröger–Vink notation. In its use as OSC, ceria is usually combined with other oxides, such as ZrO_2, to gain stability upon sintering and lower the temperature of redox conversion. More recently, mixing with praseodymium oxides has been tried to further improve the oxygen storage capacity of Ce–based compounds, taking benefit of the Pr redox reaction analogous to that of ceria, $2Pr^{4+} + O_O^x \leftrightarrows 2Pr^{3+} + ½O_2(g) + V_O^{\bullet\bullet}$ [2]. In this line, many reports have been published about OSC properties of binary or ternary solid solutions of CeO_2, ZrO_2 and PrO_x. Most of the work has been devoted to the CeO_2–PrO_x system, where it is found that doping ceria with ~50% of Pr lowers the reduction temperature from ~850 to ~450 °C[3,4].

The OSC properties of the ZrO_2–PrO_x system have also been studied, both around the pyrochlore composition $Pr_2Zr_2O_7$ as in the Pr–rich region, usually in samples synthesized by low–temperature methods [4–9]. In general, the best results (as regards for instance H_2 consumption in temperature–programmed reduction (TPR) experiments) are obtained for fluorite–like compounds with Pr contents equal to or higher than 75%. As the OSC properties of ZrO_2–PrO_x oxides rely on oxygen incorporation and release through the above redox reaction, they involve stoichiometry changes that may result in phase evolution during operation. Then, a detailed knowledge of the phase diagram (PD) allowing for redox effects is mandatory. However, some published phase diagrams still present ambiguities, especially in the high temperature sections (see Fig. S1 of supporting information) [10,11]. In this work we have undertaken a study of ZrO_2–PrO_x materials around the pyrochlore composition, produced by a laser–assisted melting and resolidification technique.

* Corresponding author.
E-mail address: sanjuan@unizar.es (M.L. Sanjuán).

https://doi.org/10.1016/j.jallcom.2022.166449

Processing has been made in four different environments: O_2, air, N_2 and 5%H_2(Ar), so as to identify the phases formed in a range of environmental conditions covering from more to less oxidising ones. The resulting phases have been characterised by means of X–ray diffraction, electron microscopy and microanalysis, magnetic susceptibility, X-ray photoelectron spectroscopy (XPS) and Raman spectroscopy, with the purpose of elucidating the structure, composition, atomic distribution and oxidation effects related to the presence of the Pr component. All these factors (in particular those related with variations in Pr oxidation state and oxygen content) are relevant for redox properties of the mixed compounds. Previous reports of $Pr_2Zr_2O_7$ pyrochlore produced by floating–zone methods have focused mainly on structural and magnetic properties [12,13].

2. Materials and methods

2.1. Synthesis of ceramic precursors

Ceramic rods of $Pr_{2\pm x}Zr_{2\mp x}O_{7\pm y}$ with different Pr content were prepared by solid state reaction. Powders of Pr_6O_{11} (purity 99.9%, Merck, Darmstaadt, Germany) and ZrO_2 (purity 99%, Merck, Darmstaadt, Germany) were sternly heated at 1200 °C and then mixed in three different ratios so as to get nominal compositions $Pr_{1.70}Zr_{2.30}O_{7+x}$ (labelled as P1.70), $Pr_2Zr_2O_{7+x}$ (PZO), and $Pr_{2.24}Zr_{1.76}O_{7+x}$ (labelled as P2.24). To compensate for the likely Pr volatilisation [12], a ~2% Pr excess was added to the nominal compositions. However, volatilisation was seen to vary with the processing atmosphere and solidification rate, being larger in oxidising atmospheres and almost negligible in neutral or reducing atmospheres at the fast processing rates used in this work. As a result, the ZrO_2/PrO_x proportion in oxidising conditions is very close to the nominal one whereas a small Pr excess remains in neutral or reducing atmospheres.

The powder mixture was then introduced in a latex tube, and shaped into a rod using a hydraulic press under a pressure of 200 MPa. After their removal from the tube, the rods were sintered at 1500 °C in air during 12 h. The brownish–colour sintered rods presented a diameter between 3 and 4 mm and were roughly 7 cm in length.

2.2. Crystal growth

Crystalline samples with a diameter of approximately 2 mm were grown, from the sintered rods, by the laser floating zone technique (LFZ) using a CO_2 laser (λ = 10.6 μm) as heating source (Blade- 600, Electronic Engineering). The growth rate was fixed at 300 mm/h, although some samples were processed at 100 mm/h to verify the influence of the growth rate in the stoichiometry and Pr oxidation sate.

In order to study the influence of the processing atmosphere on the stoichiometry and oxidation degree, samples were grown in different atmospheres (O_2, air, N_2, and 5%H_2 in Ar). The growth chamber was kept at a slight overpressure of 0.1–0.25 bar with respect to ambient pressure.

2.3. Characterization

Semi–quantitative compositional analysis and morphology were characterized by means of Field Emission Scanning Electron Microscopy (FESEM) using a Carl Zeiss MERLIN microscope with Energy Dispersive X–ray detector (EDX) incorporated.

XPS spectra were collected in a Kratos Axis SUPRA spectrometer employing a monochromatic Al Kα (1486.6 eV) X-ray source. The spectra were analysed using the CASA-XPS software. A Shirley-like baseline was used for background subtraction.

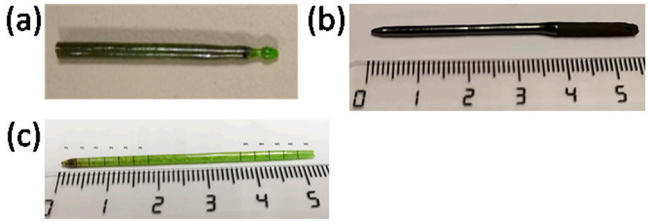

Fig. 1. PZO samples processed at 300 mm/h in 5%H_2(Ar) (a) and O_2 atmosphere (b), and at 100 mm/h in 5%H_2(Ar) (c).

The crystalline nature of the samples was analysed by powder X–ray diffraction (XRD). The data were collected with a D–Max Rigaku, Ru300 diffractometer, using the Cu K_α radiation. Patterns were measured from 5° to 70–80° with 2θ step = 0.03° and 1 or 3 s/step. Lattice parameters were determined from XRD data with the help of FullProf software [14].

Raman measurements were performed using a microprobe spectrometer (Model XY, Dilor, France) with a CCD detector. Spectra were taken at room temperature (RT) with a X50 microscope objective lens, using the 514.5 nm line of an Ar^+ laser (model Coherent INNOVA 305).

Magnetic susceptibility was obtained from magnetization measurements, under a magnetic field of 1000 Oe, performed on a SQUID detector magnetometer Quantum Design MPMS5.

3. Results

Samples with non–uniform colouration were obtained depending on the composition and processing atmosphere, a fact that may be attributed to inhomogeneity in the Pr oxidation state (Fig. 1). In Pr oxides, bright green and dark brown colours are indicative of Pr^{3+} and Pr^{4+} valence states, respectively, according to their different electronic configurations and related absorption bands in the uv–-visible spectral region. When both valence states are present, the sample adopts intermediate coloration between green and brown, depending on the Pr^{3+}/Pr^{4+} proportion. As a general rule, samples processed at 300 mm/h presented a radial colour gradient from greenish in the rod centre to brownish at the edge, this trend being more evident for samples grown in non–oxidising atmospheres. During the crystal growth process the vaporization of a brown powder takes place, especially in oxidising atmospheres. Previous work on LFZ–processed $Pr_xZr_yO_z$ compounds report it to be a praseodymium oxide. [12].

3.1. Scanning electron microscopy and EDX analysis

The microstructure of the processed $Pr_{2\pm x}Zr_{2\mp x}O_{7\pm y}$ samples was studied by Scanning Electron Microscopy (SEM) and their composition analysed by EDX. Fig. 2 shows backscattered–electron images of the transverse sections of PZO samples processed in O_2 (a) and 5% H_2(Ar) (b), and of P1.70 (c) and P2.24 (d) samples processed in 5% H_2(Ar). Other pictures can be found in Fig. S2 of the supporting information. Cation compositions determined by EDX are given in Table 1 in terms of the praseodymium molar rate (PMR, defined as the ratio between cation percentages Pr/(Pr+Zr)). Nominal PMR are 0.425, 0.50 and 0.56 for P1.70, PZO and P2.24 compositions, respectively.

P1.70 samples present large (> 100 μm) crystalline grains and a homogenous grey contrast in the whole sample (Fig. 2c; erosions in the surface are due to polishing). Accordingly, a uniform composition was found in EDX analyses, with PMR depending on the processing atmosphere (see Table 1). Lower PMR are systematically found in oxidising atmospheres in this and other compositions, which is attributed to higher Pr volatilisation. Note that a ~2% Pr

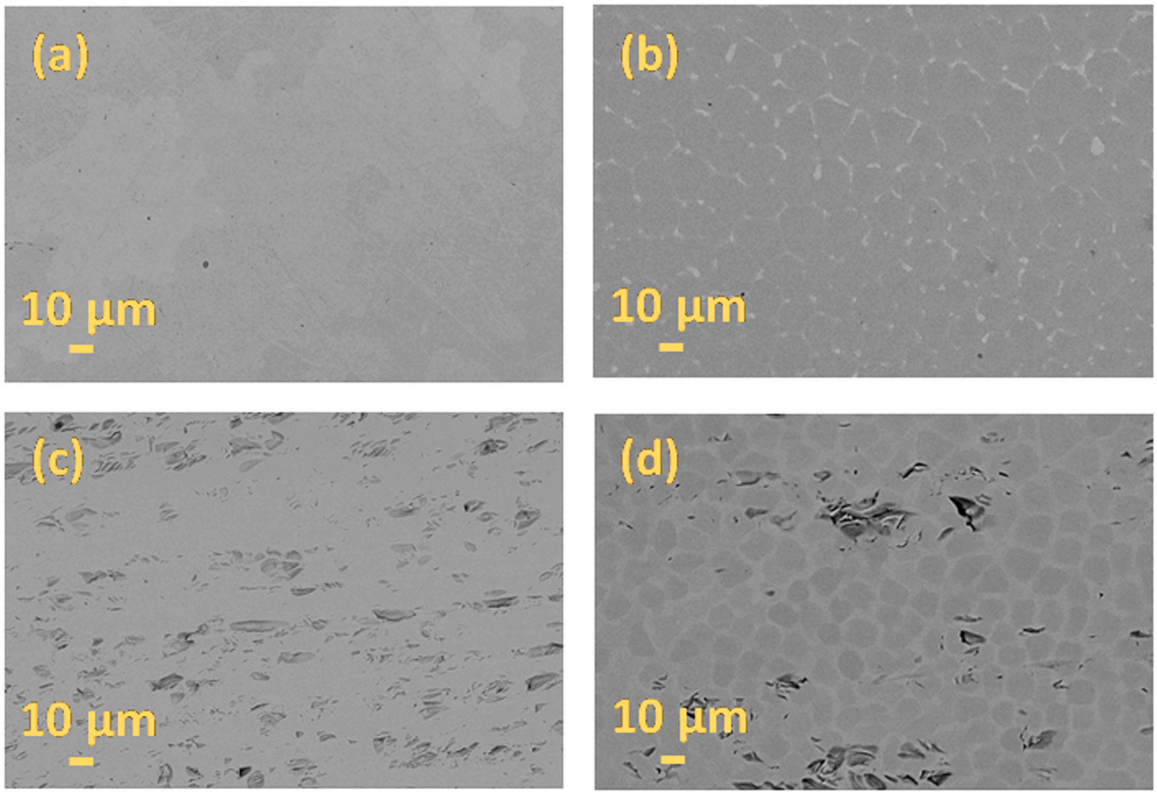

Fig. 2. Scanning Electron Microscopy images of PZO samples processed at 300 mm/h in (a) O_2 and (b) 5%H_2(Ar); (c) P1.70 processed in 5%H_2(Ar) and (d) P2.24 in 5%H_2(Ar).

excess was added to compensate for the eventual Pr loss, with the final result that samples processed in non–oxidising atmospheres present a slight Pr excess with respect to the nominal one.

At the other end, P2.24 samples display ~5–25 µm large quasi–-hexagonal grains throughout the whole transverse section, with dark and light grey contrasts at the grain centre (GC) and boundary (GB), respectively (Fig. 2d). EDX analyses showed that grain boundaries have much higher Pr content (PMR between 0.6 and 0.8) than the grain centres, and also a higher oxygen content, but a precise determination of the composition was not possible because of the narrow width (1–2 µm) of those regions, which is at the limit of EDX resolution. EBSD maps (Fig. S3) confirmed the Pr enrichment at the grain boundaries.

The "average" column in Table 1 represents measurements made over large areas (≥120 µm) so as to get a spatial average. The volume proportion of GB in Pr-rich compounds has been estimated by image analysis and is found to vary between 10% and 20%, but these numbers have to be considered just as indicative, because the GB have not precise spatial limits, neither a homogeneous composition and appear intermixed with the main (grain centre) phase.

Statistical analyses of grain sizes in different samples and atmospheres are given in Fig. S4.

The microstructure of the PZO samples is intermediate between those of P1.70 and P2.24, and depends on the processing atmosphere. Samples processed in oxidising atmospheres exhibit an inhomogeneous grey distribution at a 10–100 µm scale (Fig. 2a) and PMR ranging between 0.47 and 0.5, with average values slightly below 0.5. On the other hand, samples processed in N_2 and in 5% H_2(Ar) present two different types of regions: the first one displays large regions with slight grey contrast variation, as in Pr–poor samples, and PMR close to 0.5; the second one is formed by ~5–20 µm–sized quasi–hexagonal grains (Fig. 2b, S2 and S4), as in Pr–rich samples, with dark contrast at the grain centre (PMR ~0.5) and a narrow light–contrast phase at the boundaries with higher PMR and oxygen content.

In summary, a close correlation exists between the microstructural aspect and the average cation composition: large areas (100 µm scale) with small compositional fluctuations are found when PMR is below or at 0.5, and small grains (20 µm scale) form when the average PMR is higher than 0.5. In these grains segregation is observed between an inner region with PMR close to 0.5 and a Pr and oxygen rich outer shell with PMR reaching values of 0.8. Both types of regions can be present in the same sample, depending on the local cation composition.

Table 1
Praseodymium molar rate derived from EDX analyses of $Pr_{2\pm x}Zr_{2\mp x}O_{7\pm y}$ samples as a function of processing atmosphere. The average PMRs can be compared with nominal ones, 0.425, 0.50 and 0.56 for P1.70, PZO and P2.24 compositions, respectively, and with the actual compositions of the reagent oxide mixtures, where a 2% PrO_x excess was added to compensate for likely Pr volatilisation and thus amount to 0.433, 0.51 and 0.57 for P1.70, PZO and P2.24, respectively. H_2 stands for 5%H_2(Ar) atmosphere.

Label	O_2			Air			N_2			H_2		
P1.70	0.420			0.424			0.428			0.446		
	Range		**Aver.**	**Range**		**Aver.**	**Range**	**GC**	**Aver.**	**Range**	**GC**	**Aver.**
PZO	0.487–0.497		0.495	0.494–0.503		0.498	0.497–0.51	0.519	0.511	0.495–0.51	0.517	0.512
	GC	**GB**	**Aver.**	**GC**	**GB**	**Aver.**	**GC**	**GB**	**Aver.**	**GC**	**GB**	**Aver.**
P2.24	0.555	> 0.6	0.557	0.547	> 0.6	0.559	0.556	> 0.6	0.576	0.554	> 0.6	0.575

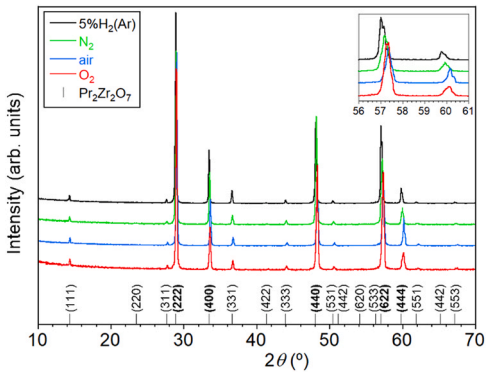

Fig. 3. X–Ray diffractograms of PZO samples processed in different atmospheres. The inset shows a magnification of the 56–61° region and the tics stand for the allowed reflections and (*hkl*) indices of the $Pr_2Zr_2O_7$ pyrochlore (*a*= 10.7099 Å), according to entry #249972 of the ICSD (Inorganic Crystal Structure Database). The main reflections, common to pyrochlore and fluorite lattices (although with doubled indices in the pyrochlore) are indicated in boldface. The remaining reflections are pyrochlore superstructure peaks.

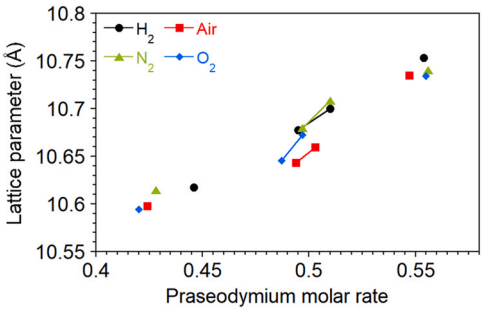

Fig. 4. Evolution of lattice parameters with the Pr molar rate determined from EDX. H_2 stands for 5%H_2(Ar) atmosphere.

3.2. X–ray diffraction

Fig. 3 shows the XRD patterns of PZO samples processed by laser floating zone at 300 mm/h in O_2, Air, N_2 and 5%H_2(Ar). The patterns of the P1.70 and P2.24 samples are shown in Figs. S5 and S6 of the supporting information.

Although the main peaks are characteristic of fluorite–like phases, the presence of weak superstructure additional peaks is indicative of pyrochlore–like phases ($Fd\bar{3}m$ space group, SG). However, most PZO and P2.24 samples evidence shoulders at the low–angle side of high–index reflections (see inset) that suggest some composition inhomogeneity, in agreement with EDX results.

An attempt has been made to determine crystallite sizes by means of the Scherrer formula, including the instrumental linewidth correction. This gives crystallite sizes $\lesssim$ 100 nm, much smaller than the size observed in SEM images. We attribute the apparent discrepancy to the peak linewidth arising not just from the crystallite size but including also other contributions, such as composition fluctuations, strain, etc., of difficult quantification.

XRD patterns were refined using the FullProf package. [14] The presence of compositional fluctuations was handled by including two close phases in the fitting procedure, when necessary, although the real situation should be more like a continuum of phases with a distribution of lattice parameters. Only one phase of pyrochlore type was required for P1.70 compositions whereas two pyrochlores were used for PZO and P2.24 samples. The requirement of two pyrochlores (and not a pyrochlore plus a fluorite phase) was ascertained from a comparison of the pyrochlore superstructure peaks fitted with either one or two pyrochlore phases (Figs. S7 and S8 of the supporting information). The assumption was further supported by the close values of the lattice parameters found for both phases. The lattice parameters obtained are listed in Table 2 and plotted in Fig. 4 as a function of the PMR determined from EDX. In drawing Fig. 4a correspondence has been established between the "phases" with low and high lattice parameters and regions with low and high Pr content found by EDX, respectively. Note that for PZO and P2.24 compositions displaying quasi–hexagonal grains no correspondence exists between the Pr–rich grain boundaries and the ad–hoc second phases introduced in the fitting. The high PMR (> 0.6) found at the grain boundaries should belong to phases with much larger lattice parameters, not expected to be of pyrochlore type. We then conclude that grain boundaries are not detected in these XRD measurements, a fact that may be ascribed to the non–uniform composition and ill crystallisation of those regions.

The gradual increase of the lattice parameters with the Pr content is in consonance with the greater size of both Pr^{3+} and Pr^{4+} compared with Zr^{4+}. Differences in the lattice parameters for a fixed composition may be attributed to variations in the Pr oxidation state. The more reducing the atmosphere, the higher the expected lattice parameter, owing to the larger ionic radius of Pr^{3+} compared to Pr^{4+}. In general, P1.70 and P2.24 samples fit to a single trend, suggesting that for these compositions Pr oxidation effects are small. For PZO samples grown in air or O_2, however, the lattice parameters are much smaller than for other atmospheres, which suggests a higher oxidation state. To elucidate the degree of Pr oxidation (and associated variation of oxygen stoichiometry) as a function of PMR and processing atmosphere we have performed magnetic susceptibility and XPS measurements, which are presented in next sections.

3.3. Magnetic susceptibility

Magnetic susceptibility measurements were performed to get a picture of the relative Pr^{3+}/Pr^{4+} proportion in processed samples, with the assumption that the effective magnetic moments derived from these data are representative of the average Pr oxidation state.

Magnetic susceptibilities of the $Pr_{2\pm x}Zr_{2\mp x}O_{7\pm y}$ samples were obtained from magnetization measurements between 1.8 K and 305 K under a magnetic field of 100 mT (Fig. S9 of the supporting information). The effective magnetic moments per Pr ion (μ_{eff}) were determined from the fit of the high temperature range (from 195 K to 305 K) of the inverse molar susceptibility to the expression $\chi^{-1} = [C/(T - \theta) + \chi_0]^{-1}$, where θ is the Curie–Weiss (CW) temperature and C is the Curie constant. The χ_0 term was added to the usual CW expression to account for the temperature–independent Van–Vleck paramagnetism [15] and was fitted by the procedure specified below. The effective magnetic moments and the relative content of

Table 2
Lattice parameters (in Å) of pyrochlore phases found in $Pr_{2\pm x}Zr_{2\mp x}O_{7\pm y}$ samples processed in different atmospheres. As explained in the text, second phases with larger lattice parameter (assigned to higher PMR) were introduced to fit the low angle tail of the diffraction peaks. H_2 stands for 5%H_2(Ar) atmosphere.

Label	O_2		air		N_2		H_2	
	Low PMR	High PMR	Low PMR	High PMR	Low PMR	High PMR	Low PMR	High PMR
P1.70	10.5941		10.5982		10.6099		10.6184	
PZO	10.6457	10.6722	10.6434	10.6595	10.6796	10.7085	10.6776	10.6998
P2.24	10.7345	10.7460	10.7348	10.7581	10.7406	10.7608	10.7535	10.7684

Pr^{3+} and Pr^{4+} ions were worked out from the relations $\mu_{eff}^2 = 8\,C$ and $\mu_{eff}^2 = \alpha\mu_{Pr3+}^2 + (1-\alpha)\mu_{Pr4+}^2$, where $\mu_{Pr3+} = 3.58\ \mu_B$ and $\mu_{Pr4+} = 2.54\ \mu_B$ are the free–ion magnetic moments of the ground–state multiplets of Pr^{3+} and Pr^{4+} ions, respectively, and μ_B is the Bohr magneton. To account for Pr volatilisation effects, the molecular mass and the number of moles in each sample were worked out using the actual cation compositions determined from EDX analyses, not from the nominal ones.

The value of χ_0 was determined as follows. First of all, we assumed that the $Pr_2Zr_2O_7$ sample solidified in 5%H_2(Ar) atmosphere at 100 mm/h, presenting a bright green colour (see Fig. 1c), contained only Pr^{3+} ions. The fit of the magnetic susceptibility of that sample to a CW term without χ_0 yielded an unreasonably large $\mu_{eff} = 3.69\ \mu_B$, and inclusion of a temperature independent term $\chi_0 = 1.8 \times 10^{-4}$ emu/mol was required to get a magnetic moment equal to the reference value of Pr^{3+}, $\mu_{eff} = 3.58\ \mu_B$. For other compositions and/or atmospheres χ_0 was fixed in a self–consistent way under the assumption that the Van Vleck correction for Pr^{4+} ions can be neglected. Then, χ_0 was varied in an iterative way until the proportion of Pr^{4+} ions resulting from the fit of the inverse molar susceptibility was coincident with the assumed Pr^{4+} content. The effective moments and χ_0 values resulting from this analysis are given in Table 3. The last column shows the percentage of Pr^{4+} ions relative to the total Pr content of each sample. With the approximations involved, the error in the Pr content is estimated to be ± 2%. The PMR column corresponds to values determined from EDX in wide areas of the samples, which average regions with high and low PMR. Fig. 5 displays the Pr^{4+} relative content as a function of the PMR.

We can first notice that for fixed composition the Pr^{4+} content depends on the processing atmosphere, so that a higher Pr^{4+} content is obtained for samples processed in oxidising atmospheres, as a general rule. For nominal P1.70 composition, the Pr^{4+} relative content is between 10% and 20%. A slightly higher percentage (13–24%) is obtained for the Pr–rich side of the pyrochlore field, nominally P2.24. However, it is somewhat surprising to find high Pr^{4+} percentages for intermediate Pr compositions (PMR ~0.5), even for those grown in 5%H_2(Ar). This is contrary to the expectation that Pr is more likely to get oxidised as PMR increases in $Pr_{2\pm x}Zr_{2\mp x}O_{7\pm y}$ compounds, as reported in previous works [6]. The Pr^{4+} content of a given sample is the result of several processes, namely oxygen diffusion across the sample, either in the melt or in the solidified rod, and oxygen release to the LFZ chamber, both depending on the processing atmosphere and sample temperature which in turn depends on the cooling rate. As we are using oxygen–rich precursors (made from Pr_6O_{11} reagents) and relatively fast solidification rates, it is not surprising that oxygen excess remains in the pyrochlores, even for those grown in reducing atmospheres. Experimental evidence supports this hypothesis: first, samples grown at 100 mm/h, such as the one shown in Fig. 1c, present a much lower or even null Pr^{4+} content. Second, annealing the P1.70 and PZO samples at 1000 °C in a vacuum resulted, independently of the processing atmosphere, in a change to green colour (see Fig. S10), as corresponds to the reduction of the existing Pr^{4+} to Pr^{3+}. A noticeable increase of the lattice parameter was accordingly observed for the most oxidised PZO sample (processed in air) after the thermal treatment in vacuum (Fig. S10). The lattice parameter change was much smaller for the P1.70 sample processed in air after the same treatment, which is attributed to the lower Pr^{4+} content in the as–prepared sample. The same treatment applied to P2.24 samples did not change the colour nor the lattice parameter, within error, which is attributed to the high stability of Pr^{4+} ions at the *B* site of Pr–rich pyrochlores, required to maintain charge neutrality without the need of oxygen vacancies. Finally, as noted before, many samples showed a colour gradient, from greenish at the centre to increasingly brownish near the edge. This trend was especially visible for samples processed in non–oxidising atmospheres. The segregation of Pr and O rich grain boundaries in PZO samples grown in reducing atmosphere was also evident (Fig. 2). We note that the Pr^{4+} percentages derived from magnetic susceptibility measurements are average values so that the presence of even small amounts of more oxidised Pr–rich regions results in higher than expected relative Pr^{4+} contents.

Table 3
Effective magnetic moment, temperature independent χ_0 term and Pr^{4+} content for $Pr_{2\pm x}Zr_{2\mp x}O_{7\pm\delta}$ samples. H_2 stands for 5%H_2(Ar) atmosphere.

	Atmosphere	PMR	$\chi_0 \cdot 10^{-4}$ (emu/mol)	μ_{eff} (μ_B)	%Pr^{4+}
P1.70	O_2	0.420	1.25	3.43	16.52
	Air	0.424	1.2	3.4	19.74
	N_2	0.428	1.3	3.46	13.27
	H_2	0.446	1.45	3.49	10.00
PZO	O_2	0.495	1.35	3.39	20.35
	Air	0.498	1.15	3.25	35.41
	N_2	0.511	1.6	3.48	10.72
	H_2	0.512	1.4	3.36	23.99
PZO 100 mm/h	H_2	0.510	1.8	3.58	–
P2.24	O_2	0.557	1.5	3.36	23.99
	Air	0.559	1.6	3.39	20.81
	N_2	0.568	1.7	3.42	17.60
	H_2	0.581	1.75	3.46	13.27

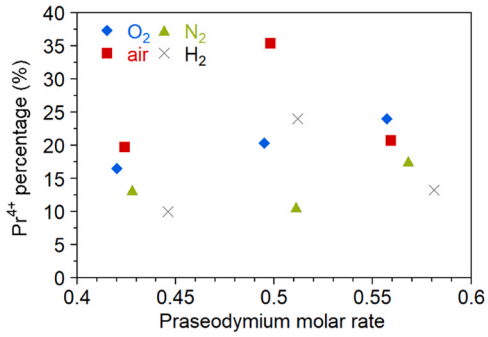

Fig. 5. Pr^{4+} percentage as a function of praseodymium molar rate for $Pr_{2\pm x}Zr_{2\mp x}O_{7\pm x}$ samples processed at different atmospheres (O_2, air, N_2, 5%H_2(Ar)).

3.4. XPS

In view of the rather high Pr^{4+} content yielded by magnetic susceptibility data in some samples, XPS spectra were recorded to validate the magnetic measurements results. Fig. 6 shows the Pr 3*d* spectra of the PZO sample processed in air at 300 mm/h. To highlight spatial variations of the oxidation state, separate measurements were taken at the rod centre and at the edge. Spectra before and after Ar sputtering were also recorded, because O 1*s* spectra (Fig. S11) evidenced the presence of additional bands around 932 eV in

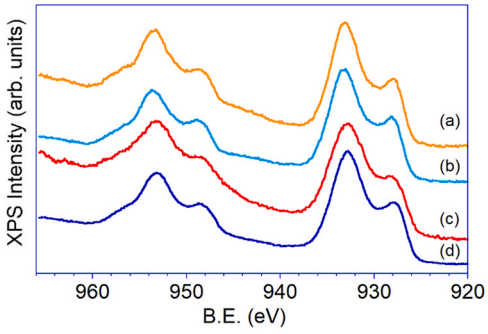

Fig. 6. XPS Pr3d spectra of PZO samples processed in air at 300 mm/h at the rod centre (a, b) and at the edge (c, d), before (a, c) and after (b, d) Ar sputtering. Spectra have been scaled for presentation purposes.

the as-prepared samples, elsewhere assigned to surface OH^- entities [17]. Binding energies (BE) were corrected according to the position of the C 1 *s* band.

Spectra in the Pr 3*d* region display the usual $3d_{3/2}$ and $3d_{5/2}$ spin-orbit-split groups of bands around 950 and 930 eV, respectively. Each group, in turn, is split into components arising from quasi-degenerate final states [16,17]. Two such components ($3\underline{d}4f^2$ and $3\underline{d}4f^3\underline{L}$) are observed for Pr^{3+} and three ($3\underline{d}4f^1$, $3\underline{d}4f^2\underline{L}$ and $3\underline{d}4f^3\underline{L}^2$) for Pr^{4+}, where $\underline{d}$ and $\underline{L}$ represent a hole in a 3*d* electronic state or in the ligand oxygen 2*p* band, respectively. Detecting Pr^{4+} relies on the weak $3\underline{d}4f^1$ components at ~946 and 966 eV [8,16,17]. Identifying those bands is difficult, however, because they overlap with other more intense bands, and depends to a great extent on the details of background subtraction, so that this procedure is only reliable for samples with a relatively high Pr^{4+} content.

To quantify the oxidation degree, data were analysed following the indications of Ref. 17, where the percentage of Pr^{4+} ions is related to the integrated intensity ratio between the band at ~946 eV and the main $3d_{5/2}$ band around 933 eV through the expression $[Pr^{4+}]/[Pr] = 3.57\ ^*I(946)/I(933)$. The intensity of the component at ~930 eV was included in the denominator, together with the main band at ~933 eV. Spectra were fitted with the help of CASA-XPS software; a Shirley-type background was subtracted and some constraints on band positions and linewidths were imposed. Examples of the fitting are given in Fig. S12. As expected, the Pr^{4+} content is lower at the sample centre (~20%) than at the rod edge (41%). Upon sputtering with Ar the OH^-–like band lowered remarkably (Fig. S11) and the Pr^{4+} decreased to 13 ± 1%, which may be ascribed to surface cleaning and to a reductive effect of Ar sputtering, respectively [17]. In summary, XPS measurements confirm the magnetic susceptibility results as regards the oxidation degree, at least for the most oxidised PZO sample.

3.5. Raman spectroscopy and oxygen stoichiometry

Raman scattering is a powerful technique for the analysis of structural anomalies in defective oxides. Compared to XRD and magnetic susceptibility, it has the advantage of providing compositional and structural information at a length scale of a few microns. Raman spectroscopy is particularly suitable to study pyrochlore–like compounds, which are prone to features such as oxygen non–-stoichiometry, cation–antisite defects and short–range–ordered domains [18]. $Pr_{2\pm x}Zr_{2\mp x}O_{7\pm y}$ compounds present the peculiarity that they may also present Pr mixed–valence effects.

The cubic pyrochlore structure of $A_2B_2O_7$ compounds (space group $Fd\bar{3}m$) can be considered a superstructure of the fluorite one with ordered cation and anion sites [19]. In a pyrochlore, cation *A* is 8–coordinated and occupies the 16*d* Wyckoff site (origin taken at *B*) while cation *B* is 6–coordinated and lays at the 16*c* site. Oxygen atoms occupy two different sites, 48*f* (O(1)) and 8*b* (O(2)), which are tetrahedrally coordinated by two *B* and two *A* cations and by four *A* cations, respectively. There is a third, unoccupied anion site, (8*a*), which is tetrahedrally coordinated to four *B* cations. The 8*a* site may be partially occupied in defect pyrochlores, either because of cation disorder or nonstoichiometry. The O(1) coordinates are (x, 1/8, 1/8), x being an indicator of how much the structure departures from the fluorite one and of the distortion at the *B* site; for $x = 0.375$ the O(1) oxygen ions occupy the fluorite–like sites, forming, together with the two 8*a* vacancies, a cube around and the *B* cation. At the other end, for $x = 0.3125$ the six O(1) around the *B* cation form a regular octahedron.

Six Raman active modes (A_{1g}, E_g, $4T_{2g}$) are expected in $A_2B_2O_7$ pyrochlores, with contribution of oxygen ions at both 48*f* ($A_{1g} + E_g + 3T_{2g}$) and 8*b* (T_{2g}) sites. *A* and *B* cations do not participate in Raman active modes, because they occupy centrosymmetric sites. Other bands are usually found in the Raman spectra of pyrochlore compounds, arising from second–order excitations, disorder effects or crystal–field transitions (see Ref. 18 and references therein).

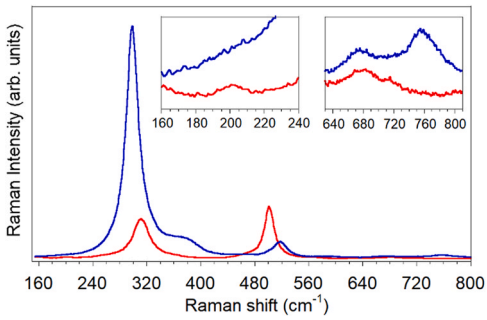

Fig. 7. Raman spectrum of $Pr_2Zr_2O_7$ single crystals at RT in *xx* (red) and *xy* (blue) configurations, where *x*, *y* stand for two perpendicular < 100 > cubic axes. The right inset displays magnified spectra to highlight a weak T_{2g} component at ~756 cm^{-1} and the left inset evidences a weak band at 200 cm^{-1} tentatively assigned to Pr^{3+} off-–centre displacements. The unpolarised band around 680 cm^{-1} is assigned to a Pr^{3+} crystal field transition.

To ease the discussion of the Raman spectra of $Pr_{2\pm x}Zr_{2\mp x}O_{7\pm y}$ compounds, we first analyse the spectrum of the stoichiometric $Pr_2Zr_2O_7$ pyrochlore. EBSD measurements (Fig. S13) show that solidification takes place along a < 100 > –like direction so that the transverse section presents a {001} plane. In such a plane, and taking *x* and *y* along two orthogonal < 100 > directions, we expect to see $A_{1g} + E_g$ modes in *xx* and T_{2g} modes in *xy* configurations. Experimental spectra (Fig. 7) yield A_{1g} and E_g modes at 501 and 312 cm^{-1}, respectively. Regarding the T_{2g} modes, three of them are clearly identified at 298, 375 and 518 cm^{-1}. The fourth T_{2g} mode of pyrochlores is controversial and has usually been ascribed either to low frequency bands around 180 cm^{-1}, as in titanates, or to a band developing at ~600 cm^{-1} in disordered pyrochlores, as in zirconates and hafnates of heavy rare earths. None of these attributions, however, agrees with recent ab–initio lattice dynamic calculations [20,21,22], which find the fourth T_{2g} at high wavenumbers (> 700 cm^{-1}), depending steeply on the *B* cation. For Zr pyrochlores it is expected around 750 cm^{-1} (Ref. 21) and in fact a close–up look at the *xy* spectrum (right inset in Fig. 7) unveils a band at 756 cm^{-1} with the correct polarisation and wavenumber that we ascribe to the fourth T_{2g} mode. We note that the band appearing at 600 cm^{-1} in disordered pyrochlores has been recently attributed to the vibration of interstitial oxygen ions occupying the 8*a* vacancy site [23,18].

Another interesting finding is the presence of a weak band around 200 cm^{-1} (left inset of Fig. 7), which cannot be attributed to an allowed mode and is neither coincident with crystal field transitions within the Pr^{3+} electronic states [24]. We propose as a likely origin of that band the presence of local Pr disorder, which would activate formally forbidden modes. Distortions in the rare–earth sublattice, either in the form of *A* atom off–centring or O(2)A_4 tetrahedra tilts, have been proposed to explain a series of X–ray, electron and neutron diffraction data of $La_2Zr_2O_7$ and $Pr_2Zr_2O_7$, and would be a means of relieving the too–short rare–earth–O(2) bond distances [12,25,26] The observation of similar bands in titanate pyrochlores has also been attributed to nominally forbidden T_{1u} modes activated by displacive disorder of the rare earth and O(2) sites [20]. Other weak features can be assigned either to second–order excitations or to crystal field transitions (CFT) between the electronic states of the $^3H_4$ ground–state multiplet of Pr^{3+} ions, in agreement with the recent identification of CFT at 77, 444, 662, 761 and 879 cm^{-1} in the Raman spectrum of PZO at 14 K (see for instance the band around 680 cm^{-1} in Fig. 7) [24]. It is interesting that off–site displacements have also been proposed in Ref. 24 to explain the split aspect of the CFT to the first excited A_{1g} state below ~150 K.

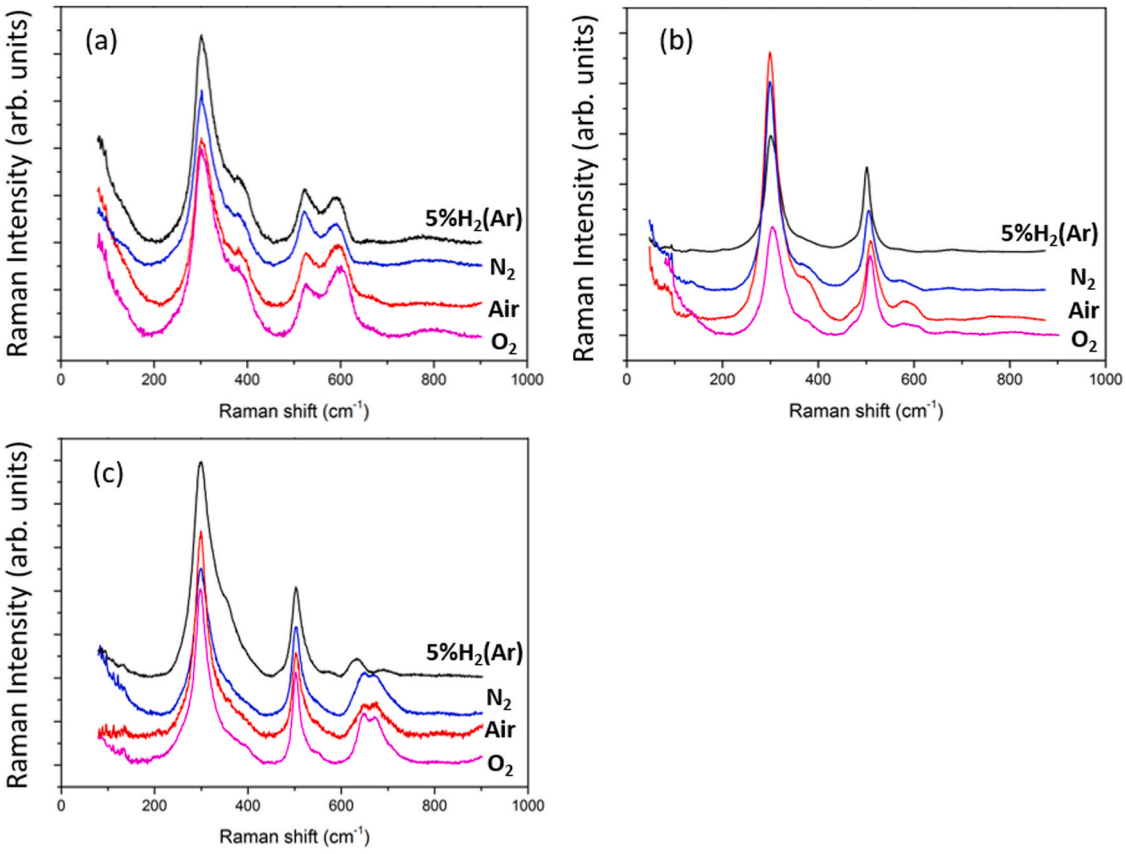

Fig. 8. Raman spectra of P1.70 (a), PZO (b), and P2.24 (c) samples processed in different atmospheres.

The two intense bands around 300 and 500 cm^{-1} are the fingerprints of the pyrochlore spectrum. The former includes contributions from the E_g mode and the first T_{2g} mode, both attributed to O(1)–*B*–O(1) bond bending [20]. The latter is assigned to the A_{1g} mode, and involves the modulation of the x_{48f} coordinate through the vibration of O(1) along the < 100 > cubic axes. The A_{1g} mode is thus sensitive to disorder effects through their influence on the environment of the *B* cation and variations of the x_{48f} parameter.

Fig. 8 shows the spectra of $Pr_{2\pm x}Zr_{2\mp x}O_{7\pm y}$ compounds as a function of composition and processing atmosphere, measured in parallel configuration along an arbitrary direction. Table 4 collects the Raman shifts of the allowed modes as a function of the composition and processing atmosphere, obtained from spectra decomposition as a sum of pseudo–Voigt profiles. Depending on the composition, additional features are observed that can be related to differences in the cation/anion stoichiometry or Pr oxidation state.

Table 4
Wavenumbers (cm^{-1}) of Raman active modes of P1.70, PZO and P2.24 samples. The experimental error is ± 1 cm^{-1}. H_2 stands for 5%H_2(Ar) atmosphere.

Sample	Atmosphere	T_{2g} (1)	E_g	T_{2g} (2)	A_{1g}	T_{2g} (3)	T_{2g} (4)
P1.70	H_2	300	323	383	523	543	
	N_2	300	320	386	522	542	
	Air	300	326	387	524	547	
	O_2	300	322	387	524	547	
PZO	H_2	299	312	375	501	518	757
	N_2	299	312	373	504	518	756
	Air	299	322	374	507	520	755
	O_2	299	317	377	505	520	
P2.24	H_2	298	324	353	503	518	755
	N_2	297	315	346	502	518	760
	Air	299	318	350	502	515	
	O_2	297	317	352	502	520	

The most noticeable feature of the spectra of P1.70 samples is the high intensity of the band at 600 cm^{-1}, regardless of the processing atmosphere. The activation of a band at that wavenumber in zirconate pyrochlores has been consistently attributed to the vibration of oxygen ions occupying the 8*a* vacant site [18,23] owing to disorder effects or non–stoichiometry. In the present case the population of the 8*a* site is required to balance out the positive charge excess arising both from the Zr^{4+} enrichment as from the presence of Pr^{4+} ions. The enhancement of the band in samples processed in oxidising atmospheres indicates a higher vacancy population, which might be attributed either to a higher Pr^{4+} proportion, in agreement with magnetic susceptibility results, or to an increase of Zr^{4+} content, because of the stronger Pr volatilisation in oxidising atmosphere. To work out the relative relevance of each of these factors we can make some numbers using the PMR derived from EDX analysis and the Pr^{4+} content deduced from magnetic susceptibility. Then, for the P1.70 sample processed in O_2, with PMR ~0.420, the stoichiometry would be $Pr_{1.68}Zr_{2.32}O_{7.16}$ in the absence of Pr oxidation, and the presence of a 16.5% of Pr^{4+} ions (0.28 per formula unit (pfu)) would imply additional 0.14 oxygen ions pfu, resulting in 0.16 + 0.14 = 0.30 total oxygen excess pfu. For the sample processed in 5%H_2(Ar) the PMR of 0.446 would give $Pr_{1.78}Zr_{2.22}O_{7.11}$ stoichiometry to which a 10% of Pr^{4+} ions (0.18 pfu) would add 0.09 oxygen atoms pfu, resulting in 0.11 + 0.09 = 0.20 total oxygen excess. Then, the ratio of expected oxygen excess (occupancy of the 8a site) between the samples processed in O_2 and in 5%H_2(Ar) is of about 1.5, which is quite close to the intensity ratio of the 600 cm^{-1} band in the corresponding Raman spectra. We thus see that i) both Pr volatilisation and Pr oxidation give comparable contributions to oxygen stoichiometry, and ii) vacancy population at the 8a site is the most likely compensation factor for Pr–poor compositions.

In PZO samples processed at 300 mm/h, the 600 cm^{-1} band is present but with weak intensity. The band appears highest for the sample processed in air. As that sample had PMR very close to 0.5, we attribute the band mainly to its high Pr^{4+} content (Fig. 8b). It is however striking that the band is very weak in the sample processed in 5%H_2(Ar), despite magnetic susceptibility yields an appreciable 24% proportion of Pr^{4+} ions. We note that the average PMR of that sample is ~0.51 and EDX showed the presence of grains with bright grain–boundaries presenting high Pr and O content. The latter are considered to be the origin of the high Pr^{4+} average content. Their inhomogeneous composition and probably bad crystallization impede to detect their Raman spectra, as occurred in X–ray diffraction. Then, the Raman spectrum shown in Fig. 8 has to be considered as representative of the more reduced, nearly stoichiometric regions.

The 600 cm^{-1} band is absent in Pr–rich P2.24 samples, suggesting that the vacancies are not or scarcely populated. This agrees with our hypothesis that in Pr–rich pyrochlores most of the Pr^{4+} ions just substitute for Zr^{4+} with no need of extra oxygen for charge compensation. However, other high–frequency bands appear in these spectra. For samples processed in air, O_2 or N_2, the high–frequency band extends from 600 to 700 cm^{-1}, and is clearly composed of at least two sub–bands at ~650 and ~670 cm^{-1}. We propose that this band is related to the large size of the Pr^{4+} ions at the octahedral sites, which induces an outward oxygen shift from the central Pr^{4+} ion resulting in shorter Zr–O bonds for nearby Zr ions.

The case of the P2.24 sample processed in 5%H_2(Ar) is interesting. At the rod centre (Fig. 8c) the spectrum displays two high frequency bands at ~630 and ~700 cm^{-1}, whereas at the rod edge the spectrum is similar to that of samples processed in the other atmospheres (Fig. S14 of supporting information). We note that according to magnetic measurements the Pr^{4+} content of that sample is ~13%, but this is an average over the central, reduced region with green colour and the brown, oxidised outer edge, and includes also the contribution from the grain boundaries. For charge neutrality and $Pr_{2.24}Zr_{1.76}O_7$ stoichiometry the Pr^{4+} content should amount to 0.24 ions pfu, i.e. 10.7% with respect to the total Pr content, whereas total Pr reduction implies an oxygen–defective $Pr_{2.24}Zr_{1.76}O_{6.88}$ pyrochlore with ~0.24 Pr^{3+} ions at the B site. We note that oxygen vacancies are proposed as the charge–balance factor of Pr–rich compositions in Ref. [9]. Then, the reduced central region of P2.24 samples processed in 5%H_2(Ar) is expected to present oxygen vacancies additional to the 8*a* ones. Since it is highly unlikely that Pr^{3+} or Zr^{4+} ions at the *B* site adopt a CN lower than 6, charge compensating vacancies may be created at the 8*b* sites. We would then find three types of Pr^{3+} environments: a majority at *A* sites with the usual 2 O(2) + 6 O(1) coordination, a small amount at *A* sites but with O(2) + 6 O(1) coordination, and those at the *B* site, coordinated with 6 O(1). The different oxygen rearrangement in these disordered configurations would explain the different high frequency bands observed in reduced P2.24 samples compared to the oxidised ones.

Fig. 9 displays Raman shifts of the allowed modes as a function of the lattice parameter. Although the A_{1g} wavenumber decreases with increasing lattice parameter (increasing Pr content), the relation is far from linear. Irrespective of the processing atmosphere, a strong decrease of the A_{1g} wavenumber is observed between P1.70 and PZO compositions, remaining approximately constant for PMR > 0.5. A similar trend is observed for the $T_{2g}(3)$ mode. All other modes present a smooth quasi–linear dependence. The evolution of the A_{1g} and $T_{2g}(3)$ modes is somewhat surprising, because the BO_6 octahedron is expected to remain more or less invariant as far as the *B* cation is Zr^{4+} (for PMR ≤ 0.5) and become expanded, on the average, for Pr rich compositions. The clue resides in the nature of the A_{1g} and $T_{2g}(3)$ modes themselves. We remind that, by symmetry, the A_{1g} mode consists of the vibration of the O(1) ions along the < 100 > directions toward the 8*a* vacancies and involves mainly O–O force constants, thus being very sensitive to the occupancy of the vacancy

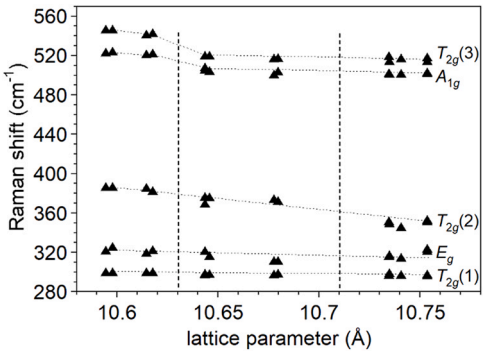

Fig. 9. Evolution of the Raman shifts of the allowed modes in the 300–550 cm^{-1} region as a function of the lattice parameter. The fourth T_{2g} mode is observed between 750 and 760 cm^{-1}. Dashed vertical lines separate data from P1.70, PZO and P2.24 samples.

sites [20]. To compensate for Zr excess, vacancies are partially populated in P1.70 compositions, which results in stronger O–O force constants and harder A_{1g} modes. Thus, the decrease of the A_{1g} wavenumber with increasing Pr content is assigned not only to lattice expansion but also to the progressive reduction of the 8*a* occupancy. Once the charge excess producing that occupancy disappears the mode frequency remains more or less constant. A similar argument explains the evolution of the $T_{2g}(3)$ modes [20–22].

Paying attention to the processing atmosphere, we can realize that for the same nominal composition samples processed in oxidising atmospheres (O_2 and air) exhibit higher Raman shifts than samples processed in N_2 or H_2, which may be attributed to the stronger volatilisation of Pr oxides in oxidising atmospheres and the resulting decrease of lattice parameter.

4. Discussion

We have performed a systematic analysis of the phases formed in the ZrO_2–PrO_x system upon melting and resolidification for compositions nominally within the pyrochlore solid–solution field, according to the published PD [10,11]. The LFZ technique has been used so as to reach the high temperatures required to melt these oxides. Four different atmospheres have been used, varying the processing conditions from oxidising to reducing.

The present results show that a close correlation exists between composition and microstructure. Two different behaviours are found, as regards phase homogeneity and microstructure, depending on whether the oxide composition is Pr–poor (PMR < 0.5) or Pr–rich (PMR > 0.5). For P1.70 compounds, homogenous microstructure and phase content are found with only smooth fluctuations of Pr rate in different areas of the sample. Raman spectroscopy suggests that occupancy of the vacancy sites (8*a*) by oxide ions is the predominant charge compensation mechanism for the excess Zr^{4+} ions, as evidenced by the detection of a band 600 cm^{-1}, consistently attributed to the vacancy population [18,23]. Oxygen located at the 8*a* site results in local Zr–O_7 coordination, which is a very stable configuration for Zr^{4+} cations. A low but non negligible Pr^{4+} content is found in these samples, even for those processed in reducing conditions. All the Pr^{4+} ions, however, can be reduced to Pr^{3+} by post–preparation thermal treatment in a vacuum. Small variations of the Pr oxidation state have little effect in the Raman spectra, except for changes in the relative amount of the 600 cm^{-1} band. A similar behaviour, as regards phase homogeneity and microstructural aspect, is observed around PMR = 0.5 (PZO samples) when there is a small Pr deficiency.

On the contrary, for PMR > 0.5 (both for P2.24 compositions as for PZO with slight Pr excess) the sample breaks into quasi–hexagonal grains composed of a pyrochlore–like phase at the grain

centre, with PMR ≤ 0.56, and a very defective and oxidised Pr–rich phase at the grain boundaries. Such a behaviour can be explained by the characteristics of the PD at the high solidification temperatures present in these experiments [10,11]. Despite pyrochlore phase admits some Pr excess, with limiting PMR = 0.56 below ~1600 °C, at high temperatures the pyrochlore solid–solution field narrows and no pyrochlore phase is stable with such composition [10,11]. Instead, separation between a Pr–poor pyrochlore phase and a Pr–rich liquid occurs, resulting in the solidification of quasi–hexagonal grains with Pr–rich grain boundaries arising from the segregated liquid. Raman scattering has provided useful information about oxygen content and location in Pr–rich samples. Two types of spectra are found, depending on the processing atmosphere: in samples processed in O_2, air or N_2 the Raman spectrum presents additional high frequency bands (but not the one at 600 cm^{-1}), which are attributed to oxygen shifts away from the Pr^{4+} ions occupying the B site, because of the larger size of this cation compared to Zr^{4+}, thus resulting in shorter Zr–O bonds with nearby Zr^{4+} ions. In contrast, the P2.24 sample processed in 5%H_2(Ar) displays a noticeable difference between spectra recorded at the rod centre (green colour, fully reduced) and at the outer region (brown colour, partially oxidised). Extra high frequency bands are observed in both cases, but at different wavenumbers. In the outer regions the spectrum is similar to that found in samples processed in oxidising atmospheres, whereas the bands found in the reduced regions are attributed to vacancies created at the 8*b* sites, to preserve at least a six–fold coordination around the Pr^{3+} ions located at the octahedral site. The radial distribution of oxygen content with enrichment toward the rod edge is attributed to incomplete outward oxygen diffusion.

As regards the variation of the Pr oxidation state, it is interesting to see that a small range of valence fluctuation is found for P1.70 and P2.24 compositions when comparing samples processed in different atmospheres, which suggests that oxygen diffusion is fast enough to release most of the oxygen excess present in the feedstock. We note that the remanence of some Pr^{4+} ions is favoured in the P2.24 compositions to avoid the creation of oxygen vacancies, but the obtained proportion of Pr^{4+} is in general higher than required for charge neutrality. Taking into account that, according to Raman spectra, no population of 8*a* sites occurs in P2.24 samples, we conclude that the excess Pr^{4+} ions are not located in pyrochlore phases but in the Pr–rich oxidised grain boundaries. The high Pr^{4+} content of the PZO composition processed in H_2 can also be understood on the same grounds, as illustrated by the difference between the samples processed at 300 and 100 mm/h: the former, presenting a Pr^{4+} relative content > 20%, had a small Pr excess and broke into grains with oxidised grain boundaries holding the Pr^{4+} ions. On the contrary, the green sample grown at 100 mm/h, with no Pr^{4+} at all, was almost exactly stoichiometric and had a very homogenous aspect with no grain segregation.

We have seen that for PMR = 0.5 and slow solidification in reducing atmosphere a stoichiometric $Pr_2Zr_2O_7$ pyrochlore is obtained. Completely reduced phases can be also obtained from P1.70 and other PZO samples by a post–synthesis annealing in reducing atmosphere or a vacuum. On the contrary, no reduction took place in Pr–rich P2.24 compositions previously containing Pr^{4+} ions, which is attributed to the high stability of the excess Pr ions at the *B* pyrochlore site in the Pr^{4+} state and the difficulty of extracting oxygen.

The present results evidence that the solidified phases depend on several factors, besides the nominal stoichiometry and processing atmosphere. First of all, it is clear that the initial oxidation state of the Pr_6O_{11} reagent is relevant for the final oxygen stoichiometry: despite the tendency of Pr to become reduced at high temperatures, kinetic factors preclude total evolution of oxygen excess and most samples remain, on the average, more oxidised than expected from nominal stoichiometry. This is especially noticeable for Pr–rich samples, whose microstructure consists of juxtaposed quasi–hexagonal grains. The physical separation between grains hampers oxygen evolution out of the grains, thus resulting in a high Pr oxidation state in the grain boundaries. A second aspect is that Pr volatilisation reduces the Pr content, especially for oxidising atmospheres, this being a function of the solidification rate: the faster the growth, the lower the volatilisation. Kinetic factors also explain the Pr content fluctuations for a given sample detected by EDX in otherwise homogenous samples and the presence of broad XRD peaks denoting a distribution of lattice parameters.

The oxygen and Pr^{4+} content pfu as well as their radial distribution are directly related to oxygen diffusivity, which is expected to vary as a function of temperature and composition. No clear conclusion has been obtained concerning this point, except for the optical evidence of darker regions (Pr^{4+}–rich) close to the edge in samples processed in reducing atmosphere and a more uniform colouration for samples processed in oxidising atmosphere, for the same solidification rate of 300 mm/h, suggesting that oxygen diffusion and release are competitive and of similar time scales. It has been reported that faster oxygen uptakes are achieved as the Pr content increases in fluorite–like ZrO_2–PrO_x mixed oxides [8]. For pyrochlore–like compositions, the oxide ion conductivity in air has been reported to vary non–monotonically as a function of Pr content, with a minimum for the 50/50 composition [9,27]. A double mechanism of oxygen diffusion in non–stoichiometric pyrochlores has been proposed, by oxygen interstitials and by vacancies, according to whether there is Pr deficiency or Pr excess, respectively [27]. In contrast, very high conductivity is found for the fluorite compound Pr_3ZrO_{7+x}, which includes a relevant proportion of electronic contribution [9,27]. In fact, differences between fluorite–like and pyrochlore–like compounds are to be expected, as regards oxygen ion conductivity. In the first case, oxygen vacancies are created in the fluorite lattice to compensate for the presence of Pr^{3+} ions. The random vacancy distribution favours oxygen conductivity, the effect increasing for intermediate Pr valence. On the contrary, in the pyrochlore lattice the ordered stoichiometric vacancies are not a source of high conductivity, which rather resides in the 48*f* sublattice [28]. Appreciable conductivity in pyrochlore compounds appears only in the case of deep cation and anion disorder (as in $Gd_2Zr_2O_7$) or if there is cation non–stoichiometry, with either rare–earth excess or deficiency, as reported in Ref. [27]. We have seen that the occupancy of the 8*a* site is the mechanism for charge compensation in our Pr–poor compounds, in which case the conduction through oxygen interstitials would apply. On the other hand, except for the sample grown in 5%H_2(Ar), our P2.24 samples contain an appreciable amount of Pr^{4+} ions, presumably at the B site, so that the lattice contains no additional vacancies other than the 8*a* ones. However, in those cases Raman measurements suggested that remarkable oxygen displacements occur around the large Pr^{4+} at *B* site, which might also enable disorder–enhanced oxygen diffusion. Pr–rich compositions belong to the "stuffed–pyrochlore" compounds where local anion disorder around the excess cations are proposed to explain their high conductivity [29]. It is clear that both Pr–rich and Pr–poor compounds have a greater cation and anion disorder than stoichiometric PZO pyrochlores, which probably explains their higher ability to release oxygen excess at high temperatures.

Finally, we would like to comment on the differences between the phases formed in the ZrO_2–CeO_x and ZrO_2–PrO_x systems processed by the LFZ technique for intermediate compositions. In the ZrO_2–CeO_x system no stable intermediate phase exists except in the fully reduced case, when the $Ce_2Zr_2O_7$ pyrochlore forms. When processing in air, a defect fluorite with cation disorder and high Ce^{4+} content is formed, yielding the well–known *t'* phase upon moderate–temperature oxidation [23,30]. When processing in reducing conditions the ordered pyrochlore $Ce_2Zr_2O_7$ is obtained, which may also be oxidised at moderate temperatures to successive metastable $Ce_2Zr_2O_{7+\delta}$ forms up to the known 2–2–8 kappa–phase, without

changing the ordered cation distribution [23,31,32]. As the trivalent oxidation state is much more stable for Pr than for Ce, no equivalent of the defect–fluorite or *t'*–phase exists in the ZrO_2–PrO_x system for intermediate compositions and a pyrochlore is always formed, even in air. For the same reason, no remarkable oxidation of the $Pr_2Zr_2O_7$ pyrochlore is feasible so that no equivalent of the kappa phase exists. The higher stability against oxidation of $Pr_2Zr_2O_7$ and its lower oxygen conductivity explain that the ZrO_2–PrO_x compositions presenting the best OSC properties are not around 50 mol% of the phase diagram, contrary to the ZrO_2–CeO_x case.

5. Summary and conclusions

We have produced crystalline samples of composition $Pr_{2\pm x}Zr_{2\mp x}O_{7\pm y}$ by laser–assisted solidification in O_2, air, N_2 and 5% H_2(Ar) atmospheres. Sample colouration changed from bright green to dark brown, owing to varying Pr^{4+} content. The most relevant result is that a close correlation exists between the phase homogeneity, the microstructure and the Pr content. For Pr molar rate (PMR) < 0.5 the samples present a homogeneous aspect, whereas Pr–rich compositions (PMR > 0.5) always break into 10–20 μm–sized grains with pyrochlore phases at the grain centre and ill–crystallised, Pr–rich oxidised phases at the grain–boundaries, coming from the segregation of Pr–rich liquid prior to solidification. Small compositional fluctuations of the pyrochlore phases are evidenced in EDX and XRD measurements, arising both from some inhomogeneity of the Pr content as of its oxidation state. An almost linear relation between lattice parameter and Pr content is found, as expected, with variations for fixed composition being attributed to differences in the Pr oxidation state.

All samples are mainly pyrochlore–like but present different types of oxygen disorder depending on composition and processing atmosphere: in Pr–poor the 8*a* vacancy is partially populated, resulting in local ZrO_7 coordination, whereas in Pr–rich samples oxygen disorder occurs around the Pr^{3+} or Pr^{4+} ions substituting for Zr^{4+}, because of size–mismatch. Magnetic measurements and XPS showed a higher–than expected Pr^{4+} content, which has been attributed to several factors: the highly oxidised state of the feedstock material, the segregation of Pr and O–rich grain boundaries in compositions with PMR > 0.5, and the lower oxide ion conductivity for PZO compositions, compared to either Pr–poor or Pr–rich compositions.

Varying the processing atmosphere affects both the cation and anion stoichiometries. Cation composition is altered because of Pr volatilisation at high temperatures, which is enhanced in oxidising atmosphere. Anion non-stoichiometry in the form of oxygen excess results from Pr oxidation, which is also favoured in oxidising atmospheres.

Credit authorship contribution statement

All the authors contributed equally to performing experimental work, data interpretation and discussion.

Data Availability

Data will be made available on request.

Declaration of Competing Interest

The authors declare that they have no known competing financial interests or personal relationships that could have appeared to influence the work reported in this paper.

Acknowledgments

We acknowledge financial support from the Spanish Government and Feder Funds (European Union) through projects MAT2016-77769R and PID2019-107106RB-C32. LG acknowledges the grant BES-2017-079683. We acknowledge the General Research Support Service of the University of Zaragoza for technical assistance in the X–ray diffraction, magnetic susceptibility and electron–microscopy measurements, and the Laboratorio de Microscopías Avanzadas (LMA) of the University of Zaragoza for technical assistance in XPS measurements.

Appendix A. Supporting information

Supplementary data associated with this article can be found in the online version at doi:10.1016/j.jallcom.2022.166449.

References

[1] Catalysis by Ceria and Related Materials, 2nd Edition, Catalytic Science Series, vol. 12, edited by Alessandro Trovarelli and Paolo Fornasiero, London: Imperial College Press, 2013.
[2] E.S. Putna, J.M. Vohs, R.J. Gorte, G.W. Graham, An examination of praseodymia as an oxygen–storage component in three–way catalysts, Catal. Lett. 54 (1998) 17–21.
[3] A.D. Logan, M. Shelef, Oxygen availability in mixed cerium/ praseodymium oxides and the effect of noble metals, J. Mater. Res. 9 (1994) 468–475.
[4] C.K. Narula, L.P. Haack, W. Chun, H.–W. Jen, G.W. Graham, Single–phase PrO_y–ZrO_2 materials and their oxygen storage capacity: a comparison with single–phase CeO_2–ZrO_2, PrO_y–CeO_2, and PrO_y–CeO_2–ZrO_2, Mater. J. Phys. Chem. B 103 (1999) 3634–3639.
[5] H. He, H.X. Dai, C.T. Au, Defective structure, oxygen mobility, oxygen storage capacity, and redox properties of RE–based (RE = Ce, Pr) solid solutions, Catal. Today 90 (2004) 245–254.
[6] J. Abel, M. Lamirand–Majimel, J. Majimel, V. Bellière–Baca, V. Harlé, G. André, C. Prestipino, S. Figueroa, E. Durand, A. Demourges, Oxygen non–stoichiometry phenomena in $Pr_{1-x}Zr_xO_{2-y}$ compounds ($0.02 < x < 0.5$), Dalton Trans. 43 (2014) 15183–15191.
[7] M.B. Bellakki, C. Shivakumara, T. Baidya, A.S. Prakash, N.Y. Vasanthacharya, M.S. Hegde, Synthesis, structure and oxygen–storage capacity of $Pr_{1-x}Zr_xO_{2-\delta}$ and $Pr_{1-x-y}Pd_yZr_xO_{2-\delta}$, Mater. Res. Bull. 43 (2008) 2658–2667.
[8] M.Y. Sinev, G.W. Graham, L.P. Haack, M. Shelef, Kinetic and structural studies of oxygen availability of the mixed oxides $Pr_{1-x}M_xO_y$ (M = Ce, Zr), J. Mater. Res. 11 (1996) 1960–1971.
[9] A.V. Shlyakhtina, J.C.C. Abrantes, E. Gomes, A.N. Shchegolikhin, G.A. Vorobieva, K.I. Maslakov, A.V. Knotko, L.G. Shcherbakova, Effect of Pr^{3+}/Pr^{4+} ratio on the oxygen ion transport and thermomechanical properties of the pyrochlore and fluorite phases in the ZrO_2–Pr_2O_3 system, Int. J. Hydrog. Energ. 41 (2016) 9982–9992.
[10] M.D. Krasil'nikov, I.V. Vinokurov, S.D. Nikitina, Physicochemical properties of solid solutions in the zirconium dioxide–praseodymium oxide system in air; in Fiz. Khim. Elektrokhim. Rasplavl. Tverd. Elektrolitov, Tezisy Dokl. Vses. Konf. Fiz. Khim. Ionnykh Rasplavov Tverd. Elektrolitov, 7th, Sverdlovsk, USSR, September 18–20, 1979, Vol. 3, pp. 123–125. Akademiya Nauk SSSR, Ural'skii Nauchnyi Tsentr, Ekaterinburg, USSR, 1979.
[11] A. Rouanet, Contribution à l'etude des systèmes zirconia—oxydes des lanthanides au voisinage de la fusion: Memoire de thèse, Rev. Intern. Hautes Temper. Refract. 8 (1971) 161–180.
[12] S.M. Koohpayeh, J.-J. Wen, B.A. Trump, C.L. Broholm, T.M. McQueen, Synthesis, floating zone crystal growth and characterization of the quantum spin ice $Pr_2Zr_2O_7$ pyrochlore, J. Cryst. Growth 402 (2014) 291–298.
[13] M.C. Hatnean, C. Decorse, M.R. Lees, O.A. Petrenko, G. Balakrishnan, Zirconate pyrochlore frustrated magnets: crystal growth by the floating zone technique, Crystals 6 (2016) 79.
[14] J. Rodriguez-Carvajal, FULLPROF: A Program for Rietveld Refinement and Pattern Matching Analysis, Abstracts of the Satellite Meeting on Powder Diffraction of the XV Congress of the IUCr, p. 127, Toulouse, France (1990).
[15] J.H. Van Vleck, A. Frank, The effect of second order Zeeman terms on magnetic susceptibilities in the rare earth and iron groups, Phys. Rev. 34 (1929) 1494–1496.
[16] A. Bianconi, A. Kotani, K. Okada, R. Giorgi, A. Gargano, A. Marcelli, T. Miyahara, Many-body effects in praseodymium core-level spectroscopies of PrO_2, Phys. Rev. B 38 (1988) 3433–3437.
[17] H. Borchert, Y.V. Frolova, V.V. Kaichev, I.P. Prosvirin, G.M. Alikina, A.I. Lukashevich, V.I. Zaikovskii, E.M. Moroz, S.N. Trukhan, V.P. Ivanov, E.A. Paukshtis, V.I. Bukhtiyarov, V.A. Sadykov, Electronic and chemical properties of nanostructured cerium dioxide doped with praseodymium, J. Phys. Chem. B 109 (2005) 5728–5738.
[18] M.L. Sanjuán, Raman spectroscopy study of disorder phenomena and size effects in pyrochlores, in Pyrochlore Ceramics: Properties, Processing and Applications,

edited by Anirban Chowdhury, Elsevier Series on Advanced Ceramic Materials, Elsevier, 2022, ISBN 9780323904834.
[19] M.A. Subramanian, G. Aravamudan, G.V. Subba Rao, Oxide pyrochlores – a review, Prog. Solid State Chem. 15 (1983) 55–143.
[20] S. Kumar, H.C. Gupta, First principles study of zone centre phonons in rare–earth pyrochlore titanates, $RE_2Ti_2O_7$ (RE = Gd, Dy, Ho, Er, Lu; Y), Vib. Spectrosc. 62 (2012) 180–187.
[21] V.A. Chernyshev, Phonon spectrum of $La_2Zr_2O_7$: ab initio calculation, Opt. Spectrosc. 127 (2019) 825–831.
[22] M. Ruminy, M. Núñez Valdez, B. Wehinger, A. Bosak, D.T. Adroja, U. Stuhr, K. Iida, K. Kamazawa, E. Pomjakushina, D. Prabakharan, M.K. Haas, L. Bovo, D. Sheptyakov, A. Cervellino, R.J. Cava, M. Kenzelmann, N.A. Spaldin, T. Fennell, First–principles calculation and experimental investigation of lattice dynamics in the rare–earth pyrochlores $R_2Ti_2O_7$ (R = Tb, Dy, Ho), Phys. Rev. B 93 (2016) 214308.
[23] P.B. Oliete, A. Orera, M.L. Sanjuán, Spectroscopic insight into the interplay between structural disorder and oxidation degree in melt–grown $Ce_{0.5}Zr_{0.5}O_{2-y}$ compounds, J. Raman Spectrosc. 51 (2020) 514–527.
[24] Yuanyuan Xu, Huiyuan Man, Nan Tang, Santu Baidya, Hongbing Zhang, Satoru Nakatsuji, David Vanderbilt, Natalia Drichko, Importance of dynamic lattice effects for crystal field excitations in the quantum spin ice candidate $Pr_2Zr_2O_7$, Phys. Rev. B 104 (2021) 075125.
[25] Y. Tabira, R.L. Withers, T. Yamada, N. Ishizawa, Annular dynamical disorder of the rare earth ions in a $La_2Zr_2O_7$ pyrochlore via single crystal synchrotron X–ray diffraction, Z. Krist. 216 (2001) 92–98.
[26] B.A. Trump, S.M. Koohpayeh, K.J.T. Livi, J.-J. Wen, K.E. Arpino, Q.M. Ramasse, R. Brydson, M. Feygenson, H. Takeda, M. Takigawa, K. Kimura, S. Nakatsuji, C.L. Broholm, T.M. McQueen, Universal geometric frustration in pyrochlores, Nat. Commun. 9 (2018) 2619.
[27] D.A. Belov, A.V. Shlyakhtina, J.C.C. Abrantes, S.A. Chernyak, G.A. Gasymova, O.K. Karyagina, L.G. Shcherbakova, Electrochemical behavior of the pyrochlore– and fluorite–like solid solutions in the Pr_2O_3–ZrO_2 system. Part I, Solid State Ion. 271 (2015) 79–85.
[28] P.J. Wilde, C.R.A. Catlow, Defects and diffusion in pyrochlore structured oxides, Solid State Ion. 112 (1998) 173–183.
[29] B.G. Mullens, Z. Zhang, M. Avdeev, H.E.A. Brand, B.C.C. Cowie, M. Saura Múzquiz, B.J. Kennedy, Effect of long– and short–range disorder on the oxygen ionic conductivity of $Tm_2(Ti_{2-x}Tm_x)O_{7-x/2}$ "Stuffed" pyrochlores, Inorg. Chem. 60 (2021) 4517–4530.
[30] M. Yashima, K. Morimoto, N. Ishizawa, M. Yoshimura, Diffusionless tetragonal–cubic transformation temperature in zirconia–ceria solid solutions, J. Am. Ceram. Soc. 76 (1993) 2865–2868.
[31] T. Omata, H. Kishimoto, S. Otsuka-Yao-Matsuo, N. Ohtori, N. Umesaki, Vibrational Spectroscopic and X–Ray Diffraction Studies of Cerium Zirconium Oxides with Ce/Zr Composition Ratio=1 Prepared by Reduction and Successive Oxidation of t'–$(Ce_{0.5}Zr_{0.5})O_2$ Phase, J. Solid State Chem. 147 (1999) 573–583.
[32] S.N. Achary, S.K. Sali, N.K. Kulkarni, P.S.R. Krishna, A.B. Shinde, A.K. Tyagi, Intercalation/deintercalation of oxygen: a sequential evolution of phases in Ce_2O_3/CeO_2–ZrO_2 pyrochlores, Chem. Mater. 21 (2009) 5848–5859.